



Single-crystalline nanotubes of spinel lithium nickel manganese oxide with lithium titanate anode for high-rate lithium ion batteries

Yuan-Li Ding^a, Bee Min Goh^b, Han Zhang^b, Kian Ping Loh^b, Li Lu^{a,*}

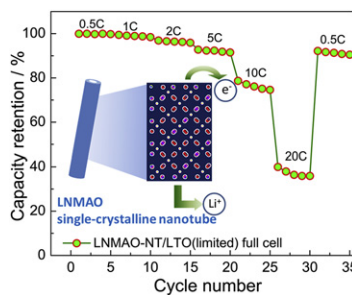
^a Department of Mechanical Engineering, National University of Singapore, 9 Engineering Drive 1, 117576 Singapore, Singapore

^b Graphene Research Centre, Department of Chemistry, National University of Singapore, 3 Science Drive 3, 117543 Singapore, Singapore

HIGHLIGHTS

- LiNi_{0.473}Mn_{1.473}Al_{0.054}O₄ single-crystalline nanotubes (LNMAO-NT) were synthesized.
- LNMAO-NT half cell exhibits capacities of 130 mAh g⁻¹ at 0.5 C and 118 mAh g⁻¹ at 5 C.
- Two types of LNMAO-NT/Li₄Ti₅O₁₂ full cells were studied by three-electrode test.
- LNMAO-NT shows superior integral structure stability upon long-term cycling.
- *In situ* Raman spectra at different potential reveal good reversibility of LNMAO-NT.

GRAPHICAL ABSTRACT



ARTICLE INFO

Article history:

Received 23 December 2012

Received in revised form

13 February 2013

Accepted 15 February 2013

Available online 26 February 2013

Keywords:

Lithium nickel manganese oxide

Single-crystalline

Nanotubes

Lithium ion batteries

ABSTRACT

Single-crystalline nanotubes of LiNi_{0.473}Mn_{1.473}Al_{0.054}O₄ (LNMAO-NT) have been synthesized and evaluated as cathode using LNMAO-NT/Li half cell and LNMAO-NT/Li₄Ti₅O₁₂ (LTO) full cell, respectively. Galvanostatic charge/discharge tests show that the LNMAO-NT half cell exhibits discharge capacity of 118 mAh g⁻¹ and specific energy (calculated only based on the cathode material) of 508 Wh kg⁻¹ at 5 C. Two types of full cells (LTO-limited and LNMAO-NT-limited cell) are constructed using three-electrode configuration. Measurement results reveal that LTO-limited full cell has a lower cathode potential vs. Li metal than LNMAO-NT-limited one at the end of cutoff voltage. The LNMAO-NT/LTO full cell exhibits discharge capacity of 158 mAh g⁻¹ at 0.5 C and 120 mAh g⁻¹ at 10 C, respectively, showing superior high-rate capability of LNMAO-NT. In addition, 87% of capacity retention of the LNMAO-NT/LTO full cell can be achieved after 200 cycles at 5 C, indicating good structural stability of one dimensional LNMAO-NT. Moreover, study of *in situ* Raman spectra at different potentials reveals good structural reversibility during charging and discharging process, indicating that LNMAO-NT would be one of the most promising high-voltage cathodes for high power lithium ion batteries.

© 2013 Elsevier B.V. All rights reserved.

1. Introduction

Improving specific energy through developing high-voltage and high capacity cathode materials and enhancing cell safety for lithium ion batteries (LIBs) has now become one of the main research directions [1–5]. To achieve these goals, more stable and reliable cathode and anode should be developed. Many high-

* Corresponding author. Tel.: +65 65162236; fax: +65 67791459.

E-mail addresses: luli@nus.edu.sg, mpeluli@nus.edu.sg (L. Lu).

voltage cathode materials have been developed in order to meet more demanding requirements of some large energy storage systems, such as electric vehicles (EVs) and hybrid electric vehicles (HEVs). At the present, some high-voltage materials are mainly focused on poly-anion compounds and Mn-based spinel oxides, such as, LiCoPO₄ (4.8 V vs. Li/Li⁺) [6], LiCoAsO₄ (4.6 V vs. Li/Li⁺) [7], LiMn_{1/3}Fe_{1/3}Co_{1/3}PO₄ (4.9 V vs. Li/Li⁺) [8], Li₂CoPO₄F (close to 5 V vs. Li/Li⁺) [9], and LiNiPO₄F (close to 5.3 V vs. Li/Li⁺) [10], LiM_xMn_{2-x}O₄ spinels (M = Ni, Cr, Fe, Co, Mg, Cu) [11–16], etc. As for poly-anion cathodes, they possess relatively lower electric and ionic conductivity, which will increase polarization during Li⁺ ions intercalation/de-intercalation process [17,18]. In addition, electrochemical activity of some poly-anion compounds has not yet experimentally understood due to high electrode potentials [10]. Compared to these poly-anion compounds, Mn-based LiM_xMn_{2-x}O₄ spinels (M = Ni, Cr, Fe, Co, Mg, Cu, etc) gain great attention because of their high electronic and ionic conductivity and easy fabrication [11–16]. The three dimensional Li⁺ ions diffusion pathways in the spinel are also beneficial to provide a high power density. Among them, non-Ni-based LiM_xMn_{2-x}O₄ (M = Cr, Fe, Co) spinels generally exhibit two voltage plateaus at 4.0 and 5.0 V vs. Li/Li⁺. High voltage beyond 5.0 V, however, will result in the fast decomposition of electrolyte [19], and hence in poor performance. Thus, LiNi_{0.5}Mn_{1.5}O₄ (LNMO) becomes a compromised target for high-voltage cathode materials because LNMO exhibits a relatively lower dominant voltage plateau at 4.7 V vs. Li/Li⁺ than other LiM_xMn_{2-x}O₄ (M = Cr, Fe, Co) spinels. In addition, it has also some advantages, such as low cost, environmental friendliness, abundant Mn resources and high thermal stability up to 250 °C [20]. Owing to its high operating voltage, LNMO can deliver a specific energy of about 650 Wh kg⁻¹, about 20%–30% higher than that of conventional LiCoO₂ (3.9 V vs. Li/Li⁺), LiMn₂O₄ (4.0 V vs. Li/Li⁺) and LiFePO₄ (3.4 V vs. Li/Li⁺), respectively. Thus, LNMO has been considered as one of the most promising high-voltage cathode materials for high power LIBs [1,21].

There still exists several problems in practical application of LNMO: i) high redox couple of Ni³⁺/Ni⁴⁺ that will result in the decomposition of conventional electrolyte based on organic carbonate and ii) difficulty in synthesis of pure LNMO spinel because of mixed ordered and disordered LNMO phases due to oxygen deficiency caused by high-temperature calcination [19,22]. Moreover, the Li_xNi_{1-x}O impurity forms probably as the second phase. Actually, it is easily obtained for disorder phase compared with stoichiometric LNMO (ordered phase with P4₃2 space group) [23]. It has been demonstrated that the disordered spinel can deliver a better electrochemical performance than ordered one because the disordered spinel has an increased Li⁺ ions diffusion coefficient [24,25]. The presence of a small amount of high spin Mn³⁺ in the disordered spinel, however, will also incur a non-negligible capacity decay during cycling, especially at elevated temperature. Thus, metal doping is generally considered as an effective approach to improve the average oxidation valence of Mn in the spinel [26–28]. Moreover, Mn³⁺ concentration in the spinel can be also decreased by re-annealing, which can also reduce oxygen defect and impurity amount, leading to better electrochemical performance [29,30].

In recent years, the charge/discharge rate capability becomes important for high power application. In order to achieve high-rate capability, nanostructured LNMO materials are widely used. Bruce and Shaju reported LNMO nanoparticles, showing superior rate capability [25]. Hernan reported that Rod-like LNMO consisted with ca. 20 nm nanocrystals synthesized based on a PEG-assisted method delivered about 90 mAh g⁻¹ of capacity at 2 C after 100 cycles, higher than counterpart (about 80 mAh g⁻¹) synthesized without adding PEG [31]. Among the various nanostructured

materials, one dimensional (1D) single-crystalline nanostructure is extremely attractive because 1D single-crystalline materials with well-defined geometry and perfect crystallization exhibit less aggregation compared with nanoparticles and are beneficial to the electronic conduction and ionic diffusion in the solid [32–34]. We have demonstrated that 1D single-crystalline LiMn₂O₄ nanotubes show the excellent electrochemical performance and superior integral stability upon long-term cycling [35]. To date, 1D single-crystalline structure of LNMO is seldom reported since it is very difficult to grow along 1D direction owing to its cubic crystal structure.

Herein we report single-crystalline nanotubes of lithium nickel manganese oxide based on our previous work [35]. The synthesized LiNi_{0.473}Mn_{1.473}Al_{0.054}O₄ (LNMAO-NT) is evaluated as cathode using LNMAO-NT/Li half cell and LNMAO-NT/Li₄Ti₅O₁₂ (LTO) full cell. The results indicate the LNMAO-NT shows superior high-rate capability, high specific energy and good cycling stability.

2. Experimental

β -MnO₂ nanotubes were firstly synthesized similar to our previous work [35]. In a typical process, stoichiometric amounts of nickel nitrate ($\text{Ni}(\text{NO}_3)_2 \cdot 6\text{H}_2\text{O}$, 0.644 mmol), aluminum nitrate ($\text{Al}(\text{NO}_3)_3 \cdot 9\text{H}_2\text{O}$, 0.068 mmol) and lithium nitrate (LiNO_3 , 3% excess, 1.397 mmol) based on the designed composition of $\text{LiNi}_{0.475}\text{Mn}_{1.475}\text{Al}_{0.05}\text{O}_4$ were firstly dissolved in deionized water (0.5 mL). Then β -MnO₂ nanotubes (2 mmol) was added into the above solution. The slurry was stirred for 4 h at 80 °C by magnetic stirring and dried at 120 °C for overnight. After grinding, the sample was calcinated at 700 °C for 10 h and subsequently annealed at 750 °C for 10 h in air at a heating rate of 2 °C min⁻¹ and a cooling rate of 1 °C min⁻¹. For comparison, micrometer-sized Al-doped $\text{LiNi}_{0.475}\text{Mn}_{1.475}\text{Al}_{0.05}\text{O}_4$ (LNMAO-M) particle was also synthesized using commercial MnO₂ based on the same fabrication process above.

The crystalline structures of LNMAO-NT were identified by X-ray diffraction using a XRD-7000 diffractometer (Shimadzu) with a Cu k_α radiation source ($\lambda = 1.5418 \text{ \AA}$). XRD data were recorded in the range $2\theta = 10\text{--}130^\circ$, with a step of 0.03° and 8 s per step. The morphology of LNMAO-NT was observed by a field-emission SEM (Hitachi S4300), TEM (JEOL 2010). The element proportion of the products was identified by inductively coupled plasma-atomic emission spectrometry (ICP-AES, ICPE 9000 Shimadzu). Raman measurements were carried out using an integrated confocal Raman microscope system (CRM 200, WITec, Germany). The instrument consists of an inverted microscope with 100×/0.9 infinity corrected objective (Olympus) for illumination and scattered light collection, allowing to reach a spatial resolution as low as 0.2 μm. An Ar⁺ laser (15 mW at 532 nm) was employed as the excitation source. The Raman microscope system operates in back-scattering mode for both excitation and collection on the same objective. The collected scattered signal was filtered to remove the contributions from excitation. Raman spectra were recorded in a back scattering geometry, and the highest grating was adopted to reach a resolution of about 1 cm⁻¹.

The electrochemical characterization of the synthesized products was performed using CR2025 coin-type cell for half and full cells. As for the full cell, LTO (Shenzhen Tianjiao corporation, Shenzhen, China) was used as anode. Three-electrode cell (ECC-REF cell, Germany) was used to evaluate the LNMAO/LTO cell with lithium metal as reference electrode. The cathode slurry was prepared by mixing LNMAO-NT, super P and polyvinylidene fluoride binder (PVDF) in a weight ratio of LNMAO-NT: Super P: PVDF = 80:10:10 in N-methyl-2-pyrrolidone (NMP). The anode slurry was the same to that of the cathode except using a weight

ratio of LTO: Super P: PVDF = 85:10:5. The blended slurries of cathode and anode were then cast onto aluminum foil and copper foil, respectively, which were dried at 80 °C 5 h in air and subsequently 120 °C overnight in vacuum oven before being pressed. LNMAO-NT was firstly investigated using two-electrode half cells (lithium metal as anode). The specific capacity of full cells is calculated by the corresponding limited electrode. For the LNMAO/LTO full cells, the limited capacity and excess capacity of the two electrodes is designed using 0.8 mAh and 1.0 mAh, respectively. In order to obtain a better alignment between cathode and anode, the diameters of the limited electrode and excess electrode are 10 and 12 mm, respectively. The loading mass of cathode is 4–6 mg cm⁻². Cell assembly was carried out in an Ar-filled glove box (MBraun). The electrolyte solution was 1 M LiPF₆ dissolved in ethylene carbonate (EC)/dimethyl carbonate (DMC)/diethyl carbonate (DEC) (1:1:1 in volume). Celgard 2400 polypropylene membrane was used as the separator. Galvanostatic charge/discharge tests were performed using Neware battery tester (Shenzhen, China). The cutoff voltages for half and full cells are 3.2–4.95 V vs. Li/Li⁺ (LNMAO-NT/Li half cell), 1.0–2.5 V vs. Li/Li⁺ (LTO/Li half cell) and 2.0–3.5 V (LNMAO-NT/LTO full cell), respectively. Cyclic Voltamograms (CVs) tests were performed on a Solartron electrochemistry workstation (Solartron 1470E) at 0.1 mV s⁻¹ using a cutoff voltage range of 3.2–4.95 V vs. Li/Li⁺ (LNMAO-NT/Li half cell), and 2.0–3.5 V (LNMAO-NT/LTO full cell). To have a convenient comparison, 1 C is defined as 140 mA g⁻¹ of current density for LNMAO-NT/Li half cell and LNMAO-NT/LTO full cell.

3. Results and discussion

Fig. 1b shows 1D tubular LNMAO-NT spinel synthesized from β -MnO₂ nanotube template as shown in Fig. 1a. The outer and inner

diameters of LNMAO-NT are about 500 and 200 nm, respectively, slightly larger than those of precursor β -MnO₂ nanotube. It is suggested that the tubes slightly swell in the direction perpendicular to the tube axis during high-temperature calcination. The length of LNMAO-NT is slightly shorter than β -MnO₂ nanotube. Fig. 1c shows magnified single LNMAO-NT from which the selected area electron diffraction (SAED) is taken from the location marked by dotted square. The high resolution TEM (HRTEM) and SAED pattern in Fig. 1d clearly reveal the single-crystalline nature of LNMAO-NT. The diffraction dots can be indexed to (220), (311) and (111) planes of cubic spinel LNMO. The lattice fringes in Fig. 1d show the high crystallinity of LNMAO-NT. These nanotubes grow preferentially along the [110] direction recorded with [112] zone axis.

The XRD pattern of LNMAO-NT shown in Fig. 2 is well indexed to a cubic LNMO spinel (JCPDS No: 80-2162), which is consistent with TEM analysis. The structure is assigned to either $P4_332$ or $Fd\text{-}3m$ space group, depending on the ordering of transition metal in the spinel structure. As for the ordered spinel, the oxidation state of Ni and Mn are +2 and +4, respectively. But for disordered spinel, a small amount of oxygen deficiency resulted by high-temperature calcination will be compensated by the formation of Mn³⁺. Many methods have been used to identify the ordered and disordered structures of the spinel material, such as XRD Rietveld analysis [36], electron diffraction [36,37], CV profiles [38,39], charge/discharge profiles [25], etc. Rietveld analysis for our sample does not show the superstructure diffraction at 15.3°, 39.7°, 45.7°, 57.5° and 65.6° [36], implying disordered spinel structure of LNMAO-NT. The refinement profiles of LNMAO-NT indicate that all peaks fit well to the $Fd\text{-}3m$ space group. The fitted structural parameters and refined results are shown in Table S1 (Supporting Information). The lattice constant is 8.166 Å, slightly smaller than stoichiometric LNMO (8.182 Å)

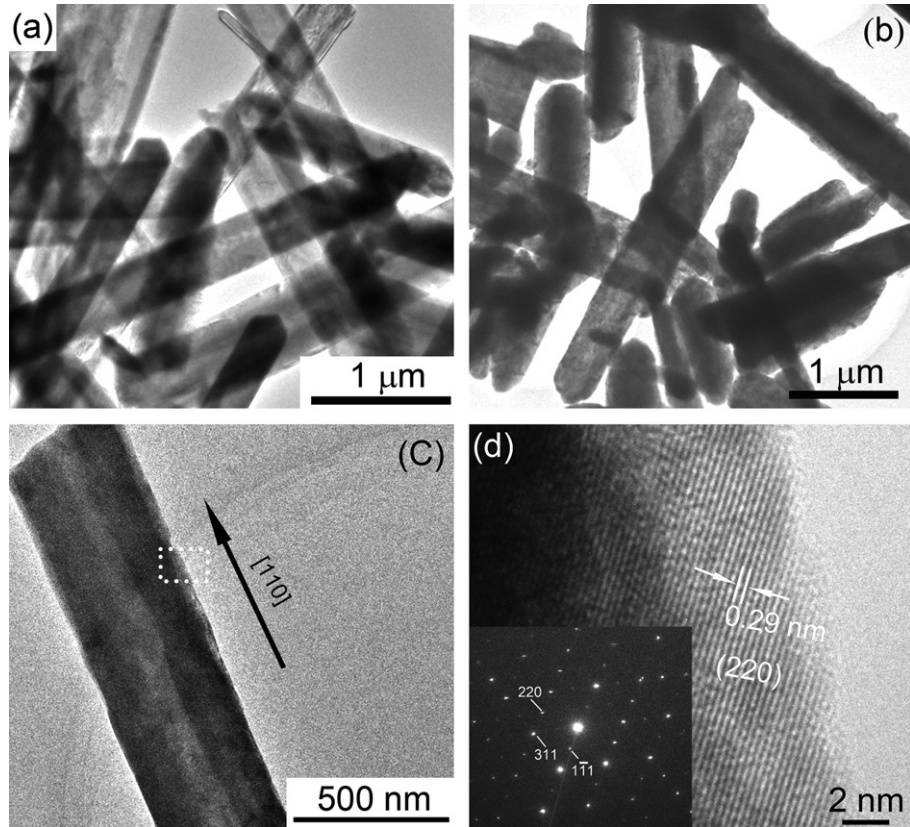


Fig. 1. TEM images of (a) β -MnO₂ nanotubes, (b) LNMAO-NT and (c) an individual nanotube of LNMAO-NT, (d) HRTEM image taken from the dotted square in (c), the inset shows the corresponding SAED pattern.

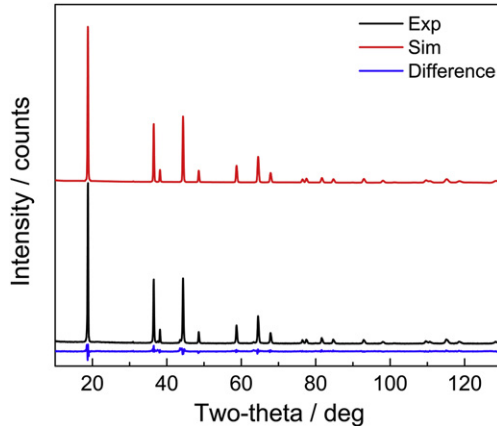


Fig. 2. Experimental (black line) and simulated (red line) XRD patterns of LNMAO-NT after Rietveld refinement in the cubic space group $Fd\text{-}3m$, $a = 8.166 \text{ \AA}$, the difference profile is shown in blue. (For interpretation of the references to color in this figure legend, the reader is referred to the web version of this article.)

owing to Al doping. ICP-AES result shows that atomic ratio of Li/Ni/Mn/Al for LNMAO-NT is 1:0.473:1.473:0.054, suggesting that the chemical formula for LNMAO-NT is probably $\text{LiNi}_{0.473}\text{Mn}_{1.473}\text{Al}_{0.054}\text{O}_4$. Considering the presence of oxygen deficiency, the accurate formula for LNMAO-NT should be $\text{LiNi}_{0.473}\text{Mn}_{1.473}\text{Al}_{0.054}\text{O}_{4-\delta}$. For convenience, $\text{LiNi}_{0.5}\text{Mn}_{1.5}\text{O}_4$ and $\text{LiNi}_{0.473}\text{Mn}_{1.473}\text{Al}_{0.054}\text{O}_4$ are used for chemical formula in this paper.

Fig. 3a shows the typical charge/discharge profiles of LNMAO-NT half cell at a current density of 20 mA g^{-1} . LNMAO-NT exhibits two voltage plateaus at 4.7 V ascribed to $\text{Ni}^{2+}/\text{Ni}^{4+}$ redox process and at about 4.0 V corresponding to the redox process of $\text{Mn}^{3+}/\text{Mn}^{4+}$. This is obviously observed at the 4.0 V area peaks marked by a dashed box in the CV profile of LNMAO-NT/Li half cell (Fig. 3b),

which further confirms the disordered spinel structure with oxygen deficiency. LNMAO-NT/Li half cell delivers a discharge capacity of about 130 mAh g^{-1} at 20 mA g^{-1} Fig. 3c shows the rate capability of LNMAO-NT at 0.5 C charge rate and different discharge rates from 0.5 to 10 C. At 0.5 C, LNMAO-NT delivers about 130 mAh g^{-1} of discharge capacity. When current rate is increased to 5 C and 10 C, LNMAO-NT delivered 115 mAh g^{-1} and 80 mAh g^{-1} of discharge capacity, higher than those of some nanoparticles [40,41]. When the current rate is decreased to 0.5 C, about 130 mAh g^{-1} of discharge capacity can still be recovered, revealing good reversibility of Li^+ ions de-intercalation/intercalation process in the 1D single-crystalline LNMAO-NT electrode. Importantly, LNMAO-NT shows higher specific energy (specific energy in this paper is calculated only based on cathode material) than LMO-NT [35]. This is a particular advantage for high-voltage LNMO spinel material. As shown in Fig. 3d, LNMAO-NT delivers above 600 Wh kg^{-1} at 1 C while LMO-NT only shows 400 Wh kg^{-1} . Even at 10 C, about 400 Wh kg^{-1} of specific energy for LNMAO-NT can still be retained.

Spinel LTO has been used as an alternative anode material for LIBs due to its good structural stability (considered as zero-strain intercalation/de-intercalation material [16,42–45]). The $[\text{Ti}_{5/3}\text{Li}_{1/3}]_{16d}\text{O}_4$ spinel framework is extremely robust and provides a three-dimensional interstitial space of face-shared 8a tetrahedral and 16c octahedral for Li^+ ion transport. What is remarkable about $\text{Li}_4\text{Ti}_5\text{O}_{12}$ electrode is that the lattice parameter and unit cell volume are essentially unchanged by lithiation, allowing fast Li^+ ion diffusion within the oxygen array. In addition, the electrochemical reaction is extremely reversible. The LNMO/LTO full cell, however, still incurs decomposition of carbonate-based electrolyte owing to high charged potential of LNMO cathode, especially at fully charged or overcharged state. In order to further investigate the electrochemical behaviors of LNMO/LTO full cell, we fabricated two types of LNMAO-NT/LTO full cell, namely LNMAO-NT-limited and LTO-limited full cells, using three-electrode cell. The schematic diagram and three-electrode testing cell are shown in Fig. 4a. LNMAO-

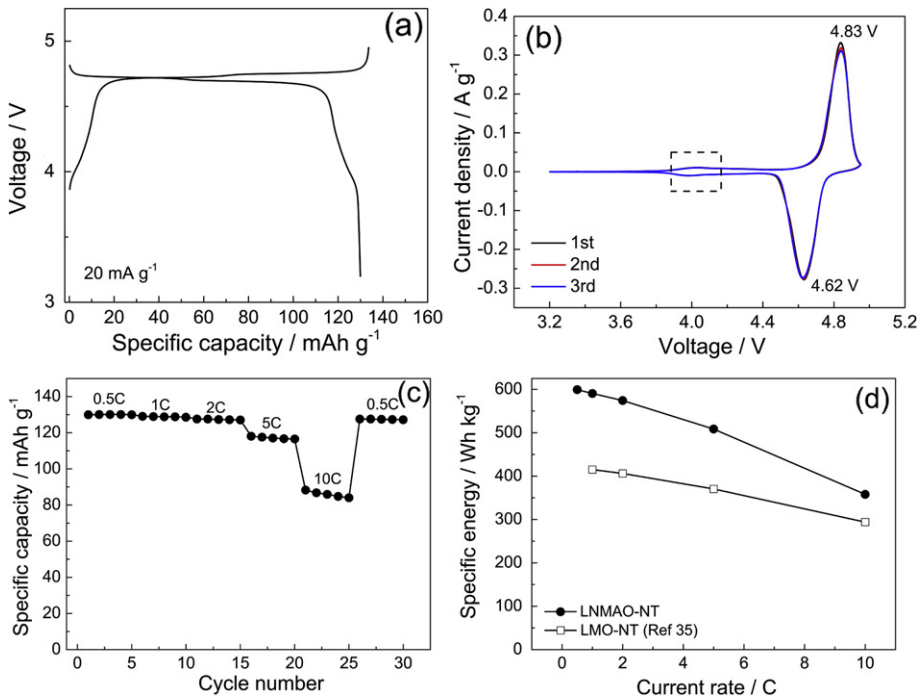


Fig. 3. (a) The typical charge/discharge profiles for LNMAO-NT/Li half cell under 20 mA g^{-1} , (b) CV plots between 3.2 and 4.95 V vs. Li/Li^+ at 0.1 mV s^{-1} , (c) the discharge capacity with cycle numbers under 0.5 C charge rate and different discharge rates for LNMAO-NT/Li half cell, (d) the specific energy with current rates for LNMAO-NT/Li and LMO-NT/Li (Ref. [35]) half cells (The specific energy is calculated only based on the mass of the cathode active materials).

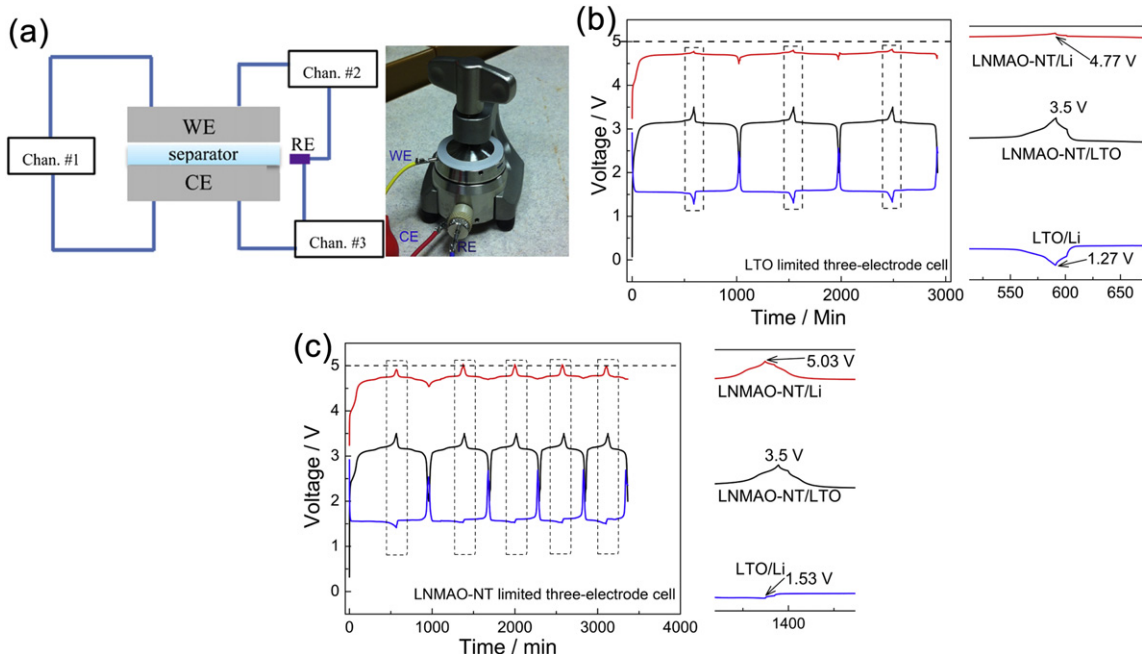


Fig. 4. (a) The schematic diagram and three-electrode cell for the three-electrode test. The charge and discharge profiles at 20 mA g⁻¹ using three-electrode cell for (b) LTO-limited and (c) LNMAO-NT-limited cells. The right part in (b) shows the magnification view corresponding the first dashed box. The right part in (c) represents the magnification view corresponding the second dashed box. The LNMAO-NT/LTO (black line) is charged and discharged between 2.0 and 3.5 V by testing Chan. #1. The response potential curves for LNMAO-NT/Li (red line, Potential/V vs. Li/Li⁺) and LTO/Li (blue line, Potential/V vs. Li/Li⁺) are simultaneously monitored by two individual testing channels (Chan.#2 and Chan. #3), respectively. The dashed boxes indicate the potential change for the LTO and LNMAO-NT-limited cells at the end of cutoff voltage. (For interpretation of the references to color in this figure legend, the reader is referred to the web version of this article.)

NT, LTO and lithium metal are used as working electrode (WE), counter electrode (CE) and reference electrode (RE), respectively. Three individual channels of battery tester are used simultaneously. Channel #1 (Chan. #1) is for charging/discharging LNMAO-NT/LTO full cell. Another two channels (Chan. #2, #3) are used to monitor the potential of LNMAO-NT/Li, and LTO/Li, respectively. Cutoff voltages of charge and discharge are set between 3.5 and 2 V for full cell system. The charge/discharge curves of the two types of full cells are shown in Fig. 4b and c. Fig. 4b shows charge/discharge curves of the LTO-limited full cell where an abrupt voltage increase from 3.2 V (plateau voltage) to 3.5 V for LNMAO-NT/LTO full cell is observed at the end of charge state. The potential for LTO drops from 1.53 V (plateau voltage) to 1.27 V vs. Li/Li⁺ while the LNMAO-NT still remains at a near plateau voltage of at 4.77 V vs. Li/Li⁺, implying that Li⁺ ions in LNMAO-NT spinel are not completely de-intercalated from the spinel structure and these Li⁺ ions extracted from LNMAO-NT can almost completely be inserted into LTO spinel structure, leading a transition from $\text{Li}_{\text{a}}[\text{Li}_{1/3}\text{Ti}_{5/3}]_{16d}\text{O}_4$ spinel to $[\text{Li}_2]_{16c}[\text{Li}_{1/3}\text{Ti}_{5/3}]_{16d}\text{O}_4$ rock-salt phase [42]. This is clearly observed from the magnification diagram corresponding to the first dashed box area in Fig. 4b. In addition, the potential values at fully charged state are maintained at about 4.7 V vs. Li/Li⁺ for subsequent cycles. In the contrast, the potential values of the LNMAO-NT-limited cell are beyond 5.0 V vs. Li/Li⁺ except the first cycle. When carefully observing the magnification view in Fig. 4c, the potential value of LNMAO-NT/Li is increased to 5.03 V vs. Li/Li⁺ while that of LTO/Li remains at a plateau voltage of 1.53 V vs. Li/Li⁺ when the LNMAO-NT/LTO cell is charged to 3.5 V. The results reveal that full cell system using LNMAO-NT-limited cell easily results in a higher potential than that of LTO-limited one. In addition, overcharge issue of LTO-limited full cell may be also alleviated because the potential of the anode can drop to 0 V along with the potential of cathode constant when the full cell is overcharged considering the zero-

strain characteristics of LTO. In contrast, the potential of cathode for LNMAO-NT-limited full cell may exceed 5.0 V or above when the cell is at overcharged state, resulting in relatively fast oxidative decomposition of electrolyte [19]. Consequently, the full cell system by the LTO-limited cell can guarantee the relatively lower potential for LNMO cathode even at its fully charged state, which is very important for alleviating the electrolyte decomposition and realizing high-rate capability and good cycling stability for LIBs.

Based on the results above, the LTO-limited full cells are further investigated. The charge/discharge curves and SEM image of LTO are shown in Fig. S1 (Supporting Information). Fig. 5a shows the initial three charge/discharge curves at 20 mA g⁻¹. It shows a dominant plateau at 3.2 V corresponding to the redox process of $\text{Ni}^{2+}/\text{Ni}^{4+}$. Another one small plateau at about 2.6 V is corresponding to the redox process of $\text{Mn}^{3+}/\text{Mn}^{4+}$. This is also clearly observed from the CV profiles marked by a dashed box in Fig. 5b, which shows a pair of sharp peaks located at 3.19/3.10 V and a pair of weak peak located at about 2.6 V. Moreover, the two-cycle CV curves show the superior reversibility of Li⁺ ions de-intercalation/intercalation process for LNMAO-NT electrode, similar to the LNMAO-NT/Li half cell (Fig. 3b). Comparing the three charge/discharge profiles (Fig. 5a), it is found that the first charge/discharge curve is obviously different from the other two. Higher charge capacity is obtained, which is due to electrolyte decomposition [46,47]. The first charge curve also displays the lower potential than the 2nd and 3rd cycle at about 2.6 V. It means that some side reactions at the electrode/electrolyte interface occur at the initial charge process, leading relatively lower potential. After the first charge/discharge cycle, a stable solid electrolyte interface (SEI) may form [48], contributing to stability of subsequent cycles. The first coulombic efficiency is only 72.4%, which is mainly attributed to the non-reversible side reaction during the first charge/discharge process [46,47]. During the subsequent cycles, above 92%

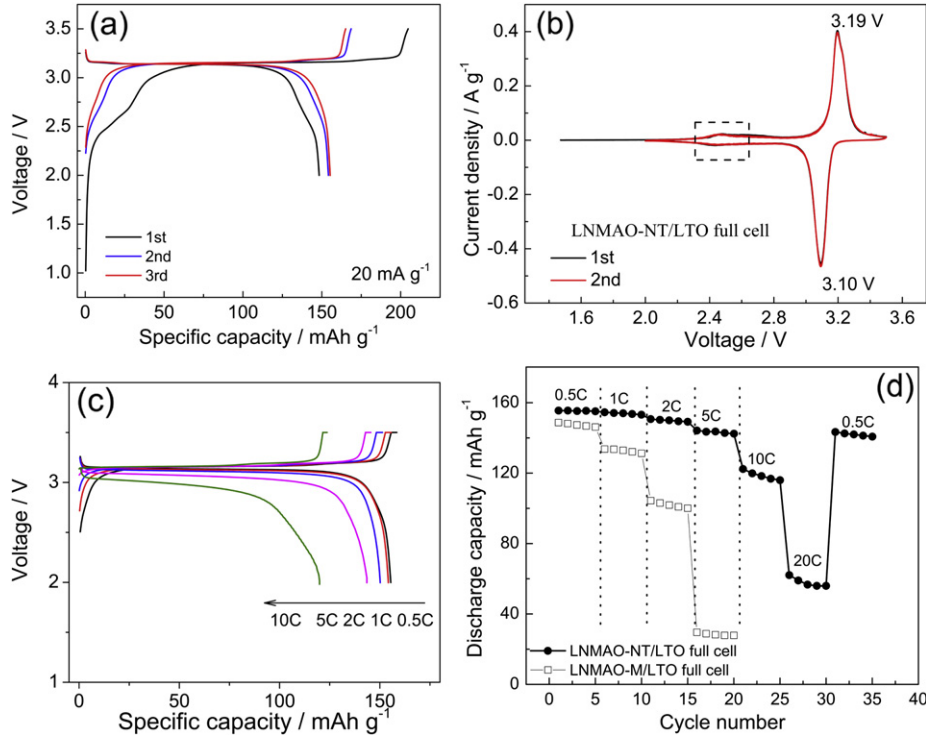


Fig. 5. (a) The initial three charge/discharge profiles for LNMAO-NT/LTO full cell at 20 mA g^{-1} , (b) CV plots for LNMAO-NT/LTO full cell between 2.0 and 3.5 V at a scan rate of 0.1 mV s^{-1} , (c) the charge/discharge curves under different discharge current rates at the same charge rate (0.5 C) for LNMAO-NT/LTO full cell, (d) Specific discharge capacity with cycle number under different current rates for LNMAO-NT/LTO and LNMAO-M/LTO full cells. Note that the specific capacity of full cell is calculated based on the limited LTO mass.

coulombic efficiency is retained because relatively stable electrode/electrolyte interface forms during the first cycle. The LNMAO-NT/LTO full cell delivers an initial discharge capacity of about 150 mAh g^{-1} at 20 mA g^{-1} (the specific capacity is calculated based on the mass of limited LTO).

Fig. 5c shows the charge/discharge profiles of the full cell charged at 0.5 C and at different discharge rate from 0.5 to 10 C. With increasing the current rate, the plateau voltage gradually shifts toward lower voltage due to the increased cell polarization at high current rate. Importantly, about 120 mAh g^{-1} of discharge capacity is still obtained at 10 C, nearly 80% of the initial discharge capacity at 0.5 C (Fig. S2, Supporting Information). Fig. 5d shows the rate capability of the full cell. When tested at a low current rate (0.5–1 C), the cell delivers a slightly higher capacity than micrometer-sized LNMAO-M. Further increasing current rate to 5 C, the capacity of LNMAO-NT shows about 5 times higher than that of LNMAO-M. Even at 20 C, about 60 mAh g^{-1} of discharge capacity can be retained. When the current rate is decreased from 20 C to 0.5 C, the discharge capacity can be well recovered to 142 mAh g^{-1} , indicating superior rate capability of LNMAO-NT.

Fig. 6 shows the retention of specific discharge capacities of the LNMAO-NT/LTO, LNMO-NT/LTO and LNMAO-M/LTO full cells. After 50 times of cycles at 5 C, the LNMAO-NT/LTO and LNMO-NT/LTO full cells respectively show 94% and 83% of capacity retention, higher than micrometer-sized LNMAO-M (74% of capacity retention), suggesting the relatively higher cycling stability of 1D single-crystalline structure. It is also found that Al-doped LNMO is more resistive to electrolyte etching than pristine counterpart due to following reasons. Al substitution on Mn sites can reduce the Jahn-Teller Mn^{3+} , leading to the improved cycling stability, which has been demonstrated from our previous work and others reported references [28,49,50]. Furthermore, Al^{3+} is easy to enter into Mn^{3+} sites during high temperature calcination because Al^{3+} has smaller

ionic radius (0.57 \AA) than Mn^{3+} (0.66 \AA). Because the Al–O bond (512 kJ mol^{-1}) is stronger than the Mn–O bond (402 kJ mol^{-1}) in the octahedron, the Al-doped LNMO is expected to have a higher structural stability, contributing to the enhanced cycling stability compared with the pristine one. Moreover, the improvement of electronic conductivity by Al doping is also responsible for the decrease of polarization effect during high-rate cycling [28]. In addition, Al substitution in the spinel structure probably promotes Ni–Mn site disorder that is shown to facilitate Li^+ ions transport, especially at high rate, leading to better high-rate cycling stability. After 200 cycles at 5 C, LNMAO-NT still remains a capacity retention of 87%, higher than LNMAO-M (47%). In order to further understand cause of cycling stability of LNMAO-NT, we performed the SEM and XRD measurement. It shows that the 1D structure can be well

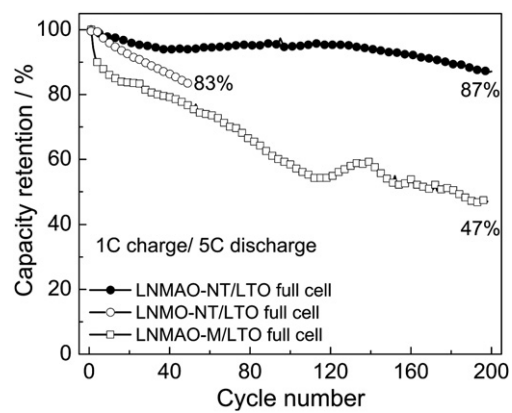


Fig. 6. The discharge capacity retention as a function of cycle number for LNMAO-NT/LTO, LNMO-NT/LTO and LNMAO-M/LTO full cells at 1 C charge/5 C discharge rate.

retained after 100 cycles at 1 C (Fig. S3, Supporting Information). The XRD pattern after cycles shows that good crystallinity can be well preserved for LNMAO-NT electrode (Fig. S4, Supporting Information). Although our LNMAO-NT shows a superior high-rate cycling stability using LTO-limited full cell system, it is inevitable for LNMO to result in the decomposition of organic carbonate-based electrolyte at a high charge voltage or fully charged state [51,52], leading to inferior long-term cycling performance. Therefore, it is necessary for enhancing the interface stability of LNMO/electrolyte to use surface modification, additives into electrolyte or more stable electrolyte in next work.

Although XRD refinement matches well with the disordered phase ($Fd\text{-}3m$ space group) for LNMAO-NT, the co-existence of ordered phase ($P4_3\text{S}2$ space group) cannot be excluded because XRD is not a sufficiently sensitive technique to distinguish the two phases. Raman spectrum is a relatively more sensitive measurement to identify some microstructure characteristics than traditional XRD method. In order to further identify the microstructural information of LNMAO-NT electrode upon different potential, *in situ* Raman spectroscopy is measured in the voltage range between 3.2 and 5.0 V vs. Li/Li⁺. Fig. 7 shows *ex situ* Raman spectra of the fresh LNMO-NT and LNMAO-NT electrodes. Compared with the Raman spectrum of the LMO-NT electrode [35], LNMO-NT displays a strong peak at 483 cm⁻¹, which is assigned to the Ni²⁺–O stretching mode in the spinel structure [53]. This band remains almost unchanged for the Al-doped LNMAO-NT sample (Fig. 7c). After charged to 5 V vs. Li/Li⁺ for the LNMAO-NT electrode, no obvious Raman shift is observed. The full width at half maximum of the band at 483 cm⁻¹ of Al-doped LNMAO-NT (Fig. 7c and d), however, becomes broader than pristine LNMO-NT. The broadening of the peak at 483 cm⁻¹ may be caused by the symmetric stretching vibration of Al–O–Al at 507 cm⁻¹ [54]. This observation implies that that Al atoms may enter into Ni sites of the spinel structure besides Mn sites, which is in good agreement with the expected result. Similar phenomena are also observed at the band located at 624 cm⁻¹, assigned to the symmetric Mn–O stretching vibration of MnO₆ octahedron. It is probably due to the presence of Al–O modes at 647 cm⁻¹ and 579 cm⁻¹ [54]. Compared with LMO-NT, LNMO-NT and LNMAO-NT present a slightly shift from 620 to 624 cm⁻¹. This shift is attributed to the increase of average oxide state of Mn and the decrease in the unit cell volume from LMO-NT to LNMO-NT or LNMAO-NT [53]. The two T_{2g} (3) splitting peaks at 580 and 595 cm⁻¹ for LNMO-NT (Fig. 7b) and at 583 and 604 cm⁻¹ for LNMAO-NT (Fig. 7c) can be clearly observed, which may be due to

the change of the Mn³⁺/Mn⁴⁺ ratio vs. Ni²⁺ in the spinel structure. In addition, T_{2g} (3) splitting peaks are often considered as the evidence of ordered spinel ($P4_3\text{S}2$) [53]. The band at 398 cm⁻¹ assigned to Ni²⁺–O stretching mode gradually becomes broad for Al-doped spinels, implying the decrease of ordered degree in spinel (Fig. 7c and d). Actually, the T_{2g} (3) splitting peaks (580 and 595 cm⁻¹) and two small peaks at 210 and 240 cm⁻¹ are the feature of ordered spinel ($P4_3\text{S}2$), implying that a little amount ordered spinel may exist for our synthesized LNMAO-NT because ordered spinel has more Raman active modes than disordered one owing to the symmetry lowering of well separated Ni and Mn sites for ordered spinel [53]. The main driving force for octahedral cation ordering is believed to be the charge difference between Ni and Mn atoms for ordered and disordered spinels. Actually, it has been reported that the laboratory-made spinel is usually a combination of two phases including ordered and disordered structures [24].

In situ Raman spectra of the LNMAO-NT sample are recorded with 532 nm excitation by using an ECC-opto cell (Fig. S5, Supporting Information). The LNMAO-NT electrode assembled in the ECC-opto cell is initially charged/discharged for 3 cycles at a low current density. Then, the electrode is firstly charged to 5.0 V vs. Li/Li⁺ and then discharged to 3.2 V vs. Li/Li⁺. Fig. 8a and b show *in situ* Raman spectra of the charge and discharge process, respectively. As shown in Fig. 8a, the LNMAO-NT electrode shows a similar Raman characteristics at an open circuit voltage of 3.97 V vs. Li/Li⁺ as the *ex situ* Raman spectra except small shifts and intensity changes of some peaks. *In situ* Raman spectra presents a higher relative intensity ($I_{\text{Ni–O}}/I_{\text{Mn–O}}$) than those measured by *ex situ* one. It is

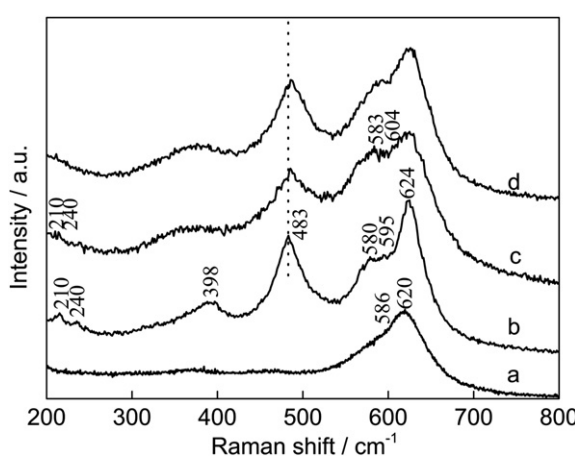


Fig. 7. *Ex situ* Raman spectra of (a) LMO-NT (Ref. [35]), (b) LNMO-NT, (c) LNMAO-NT, and (d) LNMAO-NT after charged to 5.0 V vs. Li/Li⁺.

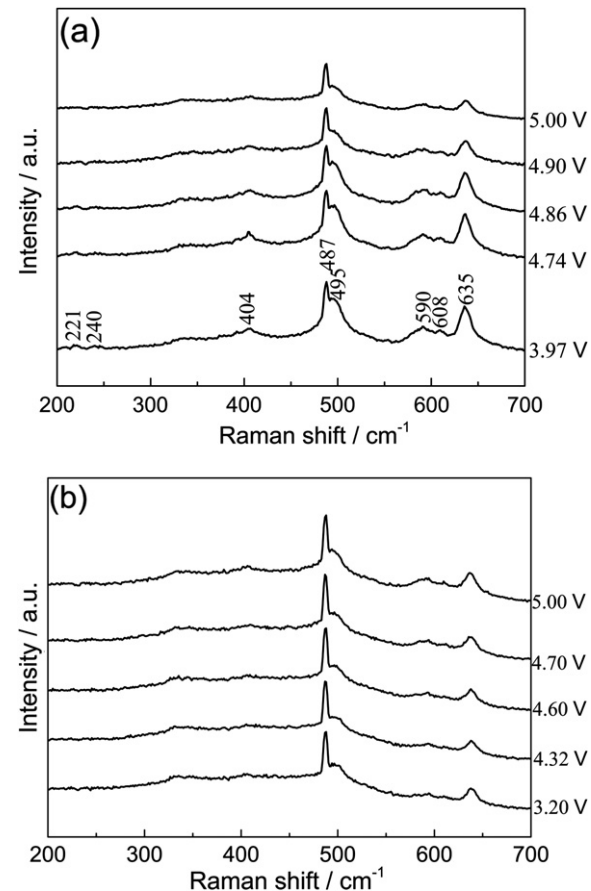


Fig. 8. *In situ* Raman spectra of LNMAO-NT/Li half cell recorded with 532 nm laser excitation: (a) the charge process from 3.97 to 5.00 V, and (b) the discharge process from 5.00 to 3.20 V.

probably ascribed to higher activity of Ni in the organic electrolyte than Mn in the spinel structure. A band at 495 cm^{-1} accompanied by the strong peak located at 487 cm^{-1} is always observed during charge and discharge process, which may be due to the presence of the LiPF_6 –EC–DMC–DEC electrolyte. This is supported from the *ex situ* spectrum of electrolyte (Fig. S6, Supporting Information), showing a weak band at 492 cm^{-1} . In addition, the intensity of the band at 495 cm^{-1} is reduced gradually with the increasing potential (Fig. 8a), especially after 4.86 V vs. Li/Li^+ , implying the occurrence of decomposition of electrolyte at a high voltage. This will result in poor cycling performance for LNMO-based cell. When discharged from 5.0 to 3.2 V vs. Li/Li^+ , the bands at 495 cm^{-1} keep basically similar peak intensity, suggesting the irreversible process of electrolyte decomposition caused by the charged process. During the whole Li^+ ions de-intercalation process from 3.97 to 5.0 V, the Raman spectra for LNMAO-NT keep almost unchanged except some intensity changes, indicating the good structure stability of LNMAO-NT electrode. It is in good agreement with the result of *ex situ* Raman (Fig. 7). It is also similar to the result of LNMO thin film reported by Mohamedi and co-workers [55]. But some small peaks at 221, 240 and 404 cm^{-1} with ordered characteristics in spinel become gradually weak and disappear with the de-intercalation of Li^+ ions from spinel, suggesting the decrease or disappearance of ordered phase during the charge process. This result implies that Li^+ ions de-intercalation from the $\text{Li}_x\text{Ni}_{0.5}\text{Mn}_{1.5}\text{O}_4$ ($P4_332$) results in a disordering from $P4_332$ to spinel $Fd\text{-}3m$, which shows the intermediate second cubic phase [36]. During the corresponding discharge process from 5.0 to 3.2 V vs. Li/Li^+ , the Raman spectra of LNMAO-NT can almost maintain similar characteristics (Fig. 8b), suggesting the good reversibility of Li^+ ions de-intercalation/intercalation from/into LNMAO-NT.

4. Conclusions

Al-doped single-crystalline nanotubes of spinel lithium nickel manganese oxide with a disordered structure ($Fd\text{-}3m$ space group) are successfully fabricated. Existence of a small amount ordered phase in spinel is also observed by *ex situ* and *in situ* Raman spectra. Galvanostatic charge/discharge measurements show that LNMAO-NT delivers superior rate capability and specific energy. Three-electrode tests reveal that the LTO-limited LNMAO/LTO full cell presents a relatively lower potential vs. lithium metal than the LNMAO-NT-limited one at the fully charged state, revealing that the full cell limited by anode has a higher tolerance to high voltage than that limited by cathode. When valued as cathode using LNMAO-NT/LTO full cell, it delivers superior rate capability and good cycling performance at relatively high rates. *In situ* Raman spectra are also used to investigate the microstructural changes upon different charging and discharging potential, revealing good reversibility during Li^+ ions de-intercalation and intercalation process. Considering its remarkably enhanced performance, single-crystalline nanotubes of Al-doped lithium nickel manganese oxide would be a very attractive high-voltage cathode material for high power and high energy application.

Acknowledgment

This work was supported by the Singapore Energy Market Authority through EPD09005RFP(A) project of Development of An Intelligent High-performance Battery System For Electric Vehicles.

Appendix A. Supplementary data

Supplementary data related to this article can be found at <http://dx.doi.org/10.1016/j.jpowsour.2013.02.047>.

References

- [1] A. Kravtsberg, Y. Ein-Eli, *Adv. Energy Mater.* 2 (2012) 922–939.
- [2] J.B. Goodenough, Y. Kim, *Chem. Mater.* 22 (2009) 587–603.
- [3] J. Song, D.W. Shin, Y.H. Lu, C.D. Amos, A. Manthiram, J.B. Goodenough, *Chem. Mater.* 24 (2012) 3101–3109.
- [4] J. Cabana, M. Casas-Cabanas, F.O. Omenya, N.A. Chernova, D.L. Zeng, M.S. Whittingham, C.P. Grey, *Chem. Mater.* 24 (2012) 2952–2964.
- [5] J. Hassoun, K.S. Lee, Y.K. Sun, B. Scrosati, *J. Am. Chem. Soc.* 133 (2011) 3139–3143.
- [6] K. Amine, H. Yasuda, M. Yamachi, *Electrochim. Solid-State Lett.* 3 (2000) 178–179.
- [7] M.V.V.M. Satya Kishore, U.V. Varadaraju, *Mater. Res. Bull.* 41 (2006) 601–607.
- [8] H. Gwon, D.-H. Seo, S.-W. Kim, J. Kim, K. Kang, *Adv. Funct. Mater.* 19 (2009) 3285–3292.
- [9] S. Okada, M. Ueno, Y. Uebou, J.-i. Yamaki, *J. Power Sources* 146 (2005) 565–569.
- [10] M. Nagahama, N. Hasegawa, S. Okada, *J. Electrochim. Soc.* 157 (2010) A748–A752.
- [11] K. Amine, H. Tukamoto, H. Yasuda, Y. Fujita, *J. Electrochim. Soc.* 143 (1996) 1607–1613.
- [12] Q.M. Zhong, A. Bonakdarpour, M.J. Zhang, Y. Gao, J.R. Dahn, *J. Electrochim. Soc.* 144 (1997) 205–213.
- [13] C. Sigala, A.L.G. La Salle, Y. Piffard, D. Guyomard, *J. Electrochim. Soc.* 148 (2001) A812–A818.
- [14] H. Shigemura, H. Sakaebe, H. Kageyama, H. Kobayashi, A. West, R. Kanno, S. Morimoto, S. Nasu, M. Tabuchi, *J. Electrochim. Soc.* 148 (2001) A730–A736.
- [15] J.S. Kim, J.T. Vaughan, C.S. Johnson, M.M. Thackeray, *J. Electrochim. Soc.* 150 (2003) A1498–A1502.
- [16] T. Ohzuku, S. Takeda, M. Iwanaga, *J. Power Sources* 82 (1999) 90–94.
- [17] B.L. Ellis, K.T. Lee, L.F. Nazar, *Chem. Mater.* 22 (2010) 691–714.
- [18] J.M. Tarascon, M. Armand, *Nature* 414 (2001) 359–367.
- [19] R. Santhanam, B. Rambabu, *J. Power Sources* 195 (2010) 5442–5451.
- [20] S.W. Oh, S.H. Park, J.H. Kim, Y.C. Bae, Y.K. Sun, *J. Power Sources* 157 (2006) 464–470.
- [21] G. Armstrong, A.R. Armstrong, P.G. Bruce, P. Reale, B. Scrosati, *Adv. Mater.* 18 (2006) 2597–2600.
- [22] T. Arunkumar, A. Manthiram, *Electrochim. Solid-State Lett.* 8 (2005) A403–A405.
- [23] J. Xiao, X. Chen, P.V. Sushko, M.L. Sushko, L. Kovarik, J. Feng, Z. Deng, J. Zheng, G.L. Graff, Z. Nie, *Adv. Mater.* 24 (2012) 2109–2116.
- [24] S. Patoux, L. Daniel, C. Bourbon, H. Lignier, C. Pagano, F. Le Cras, S. Jouanneau, S. Martinet, *J. Power Sources* 189 (2009) 344–352.
- [25] K.M. Shaju, P.G. Bruce, *Dalton Trans.* (2008) 5471–5475.
- [26] M. Akhalouch, J.M. Amarilla, R.M. Rojas, I. Saadoune, J.M. Rojo, *J. Power Sources* 185 (2008) 501–511.
- [27] S.W. Oh, S.T. Myung, H.B. Kang, Y.K. Sun, *J. Power Sources* 189 (2009) 752–756.
- [28] G. Zhong, Y. Wang, Z. Zhang, C. Chen, *Electrochim. Acta* 56 (2011) 6554–6561.
- [29] J. Tarascon, W. McKinnon, F. Coowar, T. Bowmer, G. Amatucci, D. Guyomard, *J. Electrochim. Soc.* 141 (1994) 1421–1431.
- [30] Y. Xia, H. Wang, Q. Zhang, H. Nakamura, H. Noguchi, M. Yoshio, *J. Power Sources* 166 (2007) 485–491.
- [31] J.C. Arrebola, A. Caballero, M. Cruz, L. Hernán, J. Morales, E.R. Castellón, *Adv. Funct. Mater.* 16 (2006) 1904–1912.
- [32] B. Gates, Y. Wu, Y. Yin, P. Yang, Y. Xia, *J. Am. Chem. Soc.* 123 (2001) 11500–11501.
- [33] B. Gates, B. Mayers, Y. Wu, Y. Sun, B. Cattle, P. Yang, Y. Xia, *Adv. Funct. Mater.* 12 (2002) 679–686.
- [34] Y. Xia, P. Yang, Y. Sun, Y. Wu, B. Mayers, B. Gates, Y. Yin, F. Kim, H. Yan, *Adv. Mater.* 15 (2003) 353–389.
- [35] Y.L. Ding, J. Xie, G.S. Cao, T.J. Zhu, H.M. Yu, X.B. Zhao, *Adv. Funct. Mater.* 21 (2011) 348–355.
- [36] J.H. Kim, S.T. Myung, C.S. Yoon, S.G. Kang, Y.K. Sun, *Chem. Mater.* 16 (2004) 906–914.
- [37] K.S. Ryu, Y. Lee, K.S. Han, Y.J. Park, M.G. Kang, N.G. Park, S.H. Chang, *Solid State Ionics* 175 (2004) 765–768.
- [38] A. Van der Ven, G. Ceder, *Phys. Rev. B* 59 (1999) 742–749.
- [39] B. Hwang, Y. Wu, M. Venkateswarlu, M. Cheng, R. Santhanam, *J. Power Sources* 193 (2009) 828–833.
- [40] M. Jo, Y.K. Lee, K.M. Kim, J. Cho, *J. Electrochim. Soc.* 157 (2010) A841–A845.
- [41] X. Huang, Q. Zhang, J. Gan, H. Chang, Y. Yang, *J. Electrochim. Soc.* 158 (2011) A139–A145.
- [42] T. Ohzuku, A. Ueda, N. Yamamoto, *J. Electrochim. Soc.* 142 (1995) 1431–1435.
- [43] K. Ariyoshi, S. Yamamoto, T. Ohzuku, *J. Power Sources* 119 (2003) 959–963.
- [44] H.G. Jung, M.W. Jang, J. Hassoun, Y.K. Sun, B. Scrosati, *Nat. Commun.* 2 (2011) 516–520.
- [45] H. Xiang, X. Zhang, Q. Jin, C. Zhang, C. Chen, X. Ge, *J. Power Sources* 183 (2008) 355–360.
- [46] M. Kunduraci, G. Amatucci, *J. Electrochim. Soc.* 153 (2006) A1345–A1352.
- [47] M. Kunduraci, J.F. Al-Sharab, G.G. Amatucci, *Chem. Mater.* 18 (2006) 3595–3592.
- [48] J. Arrebola, A. Caballero, L. Hernán, J. Morales, *J. Power Sources* 195 (2010) 4278–4284.

- [49] Y.L. Ding, J. Xie, G.S. Cao, T.J. Zhu, H.M. Yu, X.B. Zhao, *J. Phys. Chem. C* 115 (2011) 9821–9825.
- [50] S.T. Myung, S. Komaba, N. Kumagai, *J. Electrochem. Soc.* 148 (2001) A482–A489.
- [51] L. Yang, B. Ravdel, B. Lucht, *Electrochem. Solid-State Lett.* 13 (2010) A95–A97.
- [52] K. Xu, *Chem. Rev.* 104 (2004) 4303–4417.
- [53] N. Amdouni, K. Zaghib, F. Gendron, A. Mauger, C. Julien, *Ionics* 12 (2006) 117–126.
- [54] P. McMillan, B. Piriou, *J. Non-Cryst. Solids* 55 (1983) 221–242.
- [55] K. Dokko, M. Mohamedi, N. Anzue, T. Itoh, I. Uchida, *J. Mater. Chem.* 12 (2002) 3688–3693.